
cellSTORM – Cost-effective Super-Resolution on a Cellphone using dSTORM

Benedict Diederich^{1,2,*}, Patrick Then^{1,2}, Alexander Jügler^{1,2}, Ronny Förster^{1,2}, Rainer Heintzmann^{1,2}

1 Leibniz Institute of Photonic Technology, Albert-Einstein Str. 9, 07745 Jena, Germany

2 Institute of Physical Chemistry and Abbe Center of Photonics, Friedrich-Schiller-University Jena, Helmholtzweg 4, 07743 Jena, Germany

* benedict.diederich@ipht-jena.de

Abstract

Expensive scientific camera hardware is amongst the main cost factors in modern, high-performance microscopes. On the other hand, cheap, consumer-grade camera devices can provide surprisingly good performance. Widely available smartphones include cameras, providing a good opportunity for "imaging on a budget". Yet, Single-Molecule-Localization-Microscopy (SMLM) techniques like Photoactivated Localization Microscopy (PALM) or (direct) Stochastic Optical Reconstruction Microscopy *d*STORM, are demanding in terms of photon sensitivity and readout noise, seemingly requiring a scientific-grade camera. Here we show that super-resolution imaging by *d*STORM is possible using a consumer grade cellphone camera. Trained image-to-image generative adversarial network (GAN), successfully improves the signal-to-noise ratio (SNR) by compensating noise and compression artifacts in the acquired video-stream at poor imaging conditions.

We believe that "cellSTORM" paves the way for affordable super-resolution microscopy suitable for research and education. Our low-cost setup achieves optical resolution below 80 nm yielding wide access to cutting edge research to a big community.

Introduction

Super-resolution by Single-Molecule-Localization-Microscopy (SMLM) techniques like PALM (Photoactivated-Localization Microscopy) [1, 2] or *d*STORM [3] is well established in biology and medical research. Together with other modalities like STED [4, 5] and SIM [6, 7] SMLM revolutionized optical far-field microscopy beyond the Abbe limit [8]. Typically these methods are connected with costly hardware for excitation and detection [9, 10]. Scientific grade sCMOS or emCCD cameras are a major cost factor, as high photon efficiency and low noise are paramount.

However, the development of mobile phones created surprisingly powerful cameras and sensors, worth considering.

Almost 2.3 Billion smartphones are actively in use [11]. The effect is the availability of high quality cameras with big computational power. All that at a very low price, where each development iteration aims to further optimize not only the image quality, but also the general performance of the handheld devices [12].

This gave rise to the development of mobile microscopy, which so far resulted e.g. in hand-held devices capable of quantitative phase-imaging of biological material by combining the cellphone with customized hardware adapters [13–15] or act as portable diagnosis devices to detect e.g. waterborne parasites [15–19].

Successful attempts to image single molecules using low-cost CMOS cameras to build cost-effective SMLM setups e.g. for educational environments [10, 20, 21] demonstrate

that the imaging quality of such sensors suffices for SMLM. The small footprint and availability makes the technology suitable for educational or high bio-safety-level lab environments, as well as rapid-prototyping applications, where the processing can be done on the cellphone itself to keep size and costs small.

Commonly smartphone camera sensors, are equipped with bayer patterned filters, significantly lowering the detection efficiency compared to monochromatic imaging. Recently, some new camera modules, as in the HUAWEI P9, possess sensitive monochromatic CMOS camera chips. However, acquiring high quality RAW data using a cellphone is still very challenging. Simplified hardware abstraction layers embedded into the firmware of the camera module prevent accessing the raw pixel values. Compression and noise artifacts are therefore a potential problem of imaging with smartphone cameras.

Nevertheless, a simple adaptation of the mobile phone device a common brightfield microscope equipped with an excitation laser combination with tailored image processing algorithms should allow to gain super-resolution information well below the diffraction limit.

First, we investigate the image formation process of the smartphone camera and calibrate its noise performance. We then investigate the recovery of lost information based on machine learning approaches before we compare superresolved localization images acquired with a professional emCCD camera and a smartphone.

1 Materials and Methods

1.1 Optical setup

The basic *d*STORM-system is realized with a standard inverted microscope stand (AxioVert 135 TV, Zeiss, Germany) equipped with a nosepiece-stage (IX2-NPS, Olympus, Japan) to keep drift low. A 637 nm diode laser (P=150 mW, OBIS, Coherent, USA) is focused to the back-focal plane of the microscope objective lens (ZEISS 100 ×, NA=1.46) to realize a homogenous illumination in the sample plane. Using an adjustable mirror, it is also possible to change the laser position in the back-focal plane. This enables background-free total internal reflection (TIRF) illumination.

An emCCD camera (iXon3 DU-897, Andor, UK, Table 1) can be used to image the sample in widefield and STORM-mode during normal operation. For imaging via the cellphone, the beam-path is switched from the camera port to the eyepiece, where a common 10 × monocular eyepiece is equipped with a custom-made 3D-printed cellphone adapter [22]. The cellphone (P9 EVA-L09, HUAWEI, China, Table 1) is placed with its camera lens in the Ramsden disk of the eyepiece (see Fig 4 in Supplement A), since an eyepiece images the intermediate image produced by the tube lens of the Axiovert body to infinity. Correct imaging is assured, when the exit-pupil of the microscope is sharply imaged on the cellphone's sensor. To keep distortions like field curvature or vignetting as low as possible, we cropped the video-frames to an active area of 512 × 512 pixels around the center of the frame. Additionally the focus of the photo-lens was fixed to infinity to minimize any extra aberrations.

We use the 12 Bit monochromatic sensor chip (Sony IMX 286, Japan, Table 1, [23] of the P9's dual-camera module.

Table 1. Comparison of a scientific-grade with a low-cost cell phone camera

	Andor iXonEM+ 897	HUAWEI P9 (EVA-L09, Sony IMX286, Grayscale)
Pixel#:	512 × 512	3980 × 2460
Sensortype	(back-illuminated) emCCD	(back-illuminated) CMOS
Pixelsize (μm):	16	1,25
Bitdepth:	14 Bit	12 Bit
Read Noise (e^-):	0,2 RMS	1,23 RMS (see Supplement B)
Quantum-Efficiency	$\geq 90\%$	$\approx 70 - 80\%$

1.2 Image acquisition and reconstruction

The aim of the camera manufacturers is to ensure optimal image quality in everyday environments. Tailored algorithms help to hide problems introduced e.g. by the small pixels and lens dimensions [24, 25].

In contrast to industry-standard CMOS cameras, which mostly rely on the same sensor types, the entire post-processing of the acquired images is done by proprietary firmware on a dedicated circuit, called image signal processor (ISP) [26–28]. This allows real-time optimization of the image quality. It is mainly responsible for demosaicing the Bayer-pattern to generate RGB images, but also reduces the effect of lens aberrations and removes hot-pixels or thermal noise [24, 29]. The ISP takes also care of the hardware control (e.g. autofocus, optical image stabilization) and encoding of the video-stream into less memory consuming formats [30]. The smartphone camera is optimized for beautiful rather than accurate images, thus the scientific relevant information for SMLM of the position dependent quantity of the photons is partially lost by the on-chip processing.

1.3 Cellphone data acquisition

Cellphones of the newer generations allow to access the raw camera sensor pixel values, i.e. the sensor data before further processing or compression by e.g. JPEG/MPEG algorithms. Recording the unprocessed raw-data ("snap-mode") makes the use of cellphones even more attractive for science [17, 19, 31–33].

However, *d*STORM requires continuous (to keep the molecules in the dark state) and fast acquisition over several minutes which is incompatible with snap-mode acquisition. The computational effort to save a time-series of raw-frames makes it impracticable for these measurements.

Hence, we were forced to use the standard time-series acquisition mode ("video-mode"), where the compression of the raw data was unavoidable.

Acquiring monochromatic video-sequences is not part of the cellphone's software by default. To circumvent this issue, we wrote a customized APP (application) based on the Google Android Camera2 API [30] and an open-sourced camera library "FreeDcam" [34, 35], which enables the full control over the camera parameter like sensitivity (ISO), focus position, exposure time and frame-rate, as well as the access to the monochromatic chip.

Following the Camera2 API, the camera acts as a server which receives capture requests. These encompass hardware settings of an individual frame or sequences of images. To capture monochromatic images, the vendor-specific settings have to be accessed, hidden in the JAVA reflection classes. Once a camera request is processed, the camera yields a capture result, which has to be drawn on a surface object and can later be processed by a media recorder. In case of an Android device, the latter can be either a JPEG or DNG writer, both of which rely on hardware accelerated processing using java native interface (JNI).

Down-converting the video-stream, e.g. using the H264 video-codec, is also implemented on the ISP. To reduce the amount of memory, it relies on the exact-match integer transform [25, 36, 37] which uses reference images and calculates residual/difference images to reduce the amount of redundant information. The lossy compression incorporates accurate information of the actual pixel-values, necessary for precise localization of the fluorophores according to our experiments.

1.3.1 Neuronal networks for image enhancement

In order to reduce imaging artifacts resulting from high pixel-noise or strong compression (see Supplement A), we made an implicit black-box model (an artificial neural network) of the camera, describing the image degradation process with the aim to recover the image information prior to compression from the measured data.

Machine learning can learn an implicit model which maps a set of input variables onto a set of outputs [38–41]. A large variety of different network architectures have shown, that, resulting from prior knowledge, single-image super-resolution (interpolation) [42] or recovering the optical phase from an intensity image [43] is possible. The popular image-to-image GAN (pix2pix) [44] generates images by learning features from a set of inputs and applies it to the outputs (e.g. colorizing b/w image). Compared to former approaches, based on encoder-decoder networks [45], the cost-function for the training process is not directly defined but trained alongside the generator. This enables a customized cost-function which, fits the model better and avoids issues of blurring the generated results for example in case of the L2-norm [44, 46].

Previous approaches trained a noise model using adversarial network architectures (GAN) [41, 47] or directly localized STORM events using an auto-encoder [40] or Bayesian-statistics [48].

Here we aimed to enhance the image quality, after the raw frames of point-emitters were altered by the unknown image preprocessing and compression of the HUAWEI P9 cellphone. Following a modified version of the pix2pix network architecture (see Supplement C). The goal of the network is to recover high quality (e.g. high SNR) images (referred to "B") from degraded video-frames of real STORM measurements (referred to "A"). To produce training datasets, we developed three different methods to generate "A to B" data-pairs.

The first approach is based on purely simulated data, where blinking events are degraded based on our camera model described in in Supplement B. A second approach holds simulated *d*STORM events with known positions displayed on a secondary screen and their recorded frames from the cellphone camera. The third method takes a localized result from a real *d*STORM measurement from a cellphone and produces perfect PSFs for each frame and combines it with the noisy video frames.

It turned out, that mixing data based on the first and third method gives the best results. Further details on the generation of the dataset can be found in Supplement A.

1.4 *d*STORM imaging samples

Cell samples have been prepared from HeLa cells using the PFA-fixation protocol outlined in [49]. Microtubuli have been stained using Monoclonal mouse anti- β -tubulin (Sigma Aldrich) and Goat anti-Mouse IgG secondary antibody (ThermoFisher Scientific), labeled with Alexa Fluor 647 at 1:150 and 1:300 dilution, respectively. All imaging experiments have been conducted in imaging buffer prepared freshly from 150-200mM MEA (β -Mercapto-ethylamine hydrochloride) in PBS and pH adjusted to 7.4 using NaOH. The

oxygen scavenging effect from MEA has been proven efficient enough to refrain from additional enzyme-based oxygen scavenger systems.

2 Results

We divide the results into two parts. First, we show our localized SMLM data using a smartphone under optimal imaging conditions which are directly suitable for standard *d*STORM image processing and then we present a second less optimal dataset, where preprocessing by a NN was required to yield results of good quality.

The less optimal data set should simulate the use of cameras with less quality of not optimal chosen parameters for the acquisition process.

2.1 Localization with Compressed Smartphone Data

The reduced SNR (signal-to-noise ratio) and additional artifacts from video compression are directly apparent in the image sequences acquired by a cellphone camera. Nevertheless, the robust nature of the reconstruction algorithms enables successful localization of blinking events even under non-ideal conditions. Here, we used the freely available rapidSTORM [50] and ThunderSTORM [51] software, which yielded comparable results when reconstructing the final image from recorded data.

Figure 1 shows the results obtained with cellSTORM from HeLa cells stained for tubulin using AlexaFluor 647-labeled primary/secondary antibodies. After applying thunderSTORM directly to the ≈ 18 thousand acquired video images (at 20 fps), the structure of microtubuli is clearly resolved at a resolution of 75 nm measured using the Fourier ring correlation [52]. To compare to conventional *d*STORM data, we recorded another series of a similar cell using the emCCD camera of our setup. Due to the already low photon yield at the cellphone camera, we opted against using an beamsplitter to simultaneously record the same area with cellphone and emCCD camera and instead imaged separate cells of the same sample.

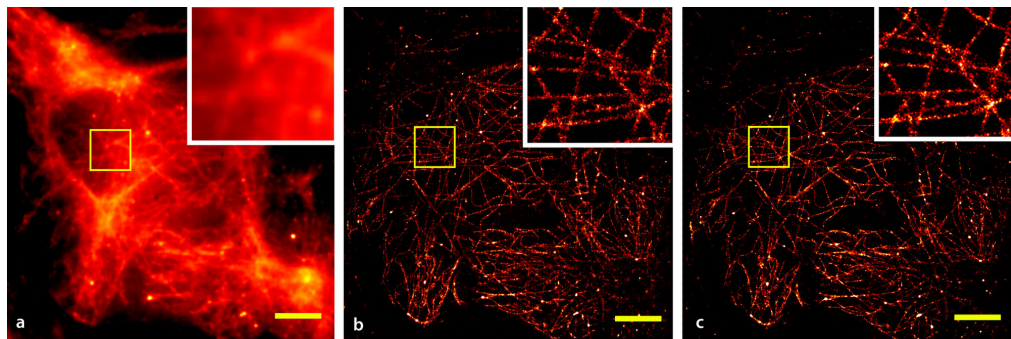


Figure 1. Microtubuli in HeLa cells stained using AlexaFluor 647 labeled antibodies and recorded with the cellphone camera after reconstruction with rapidSTORM (a) and a picture obtained through summing all recorded frames (b), equivalent to a widefield image. No drift correction was applied to the time-series. (Scalebar = $1 \mu m$)

The images acquired using the professional emCCD camera 2 under identical buffer and illumination conditions yielded a final resolution of 45 nm. While this number is smaller than for cellSTORM the relative difference is nonetheless surprisingly small.

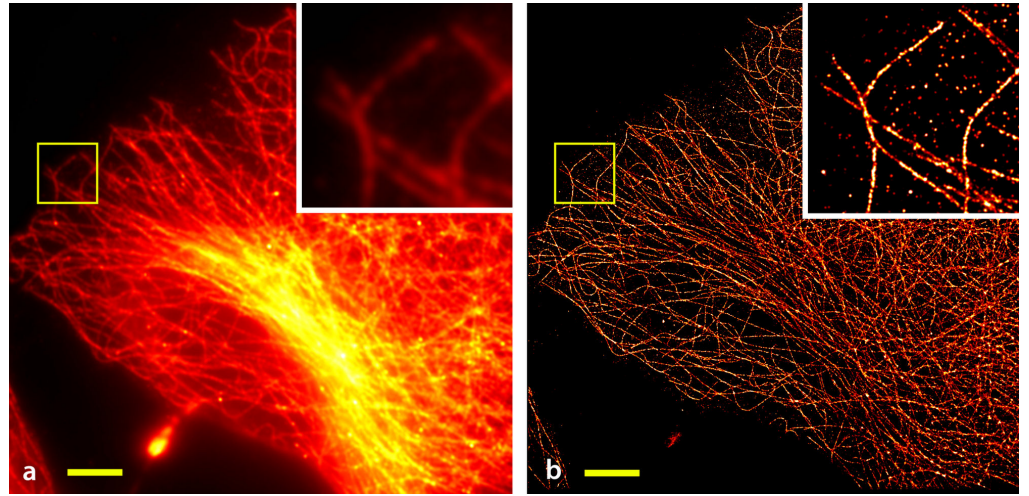


Figure 2. Microtubuli in HeLa cells stained using AlexaFluor 647 labeled antibodies and recorded with the Andor emCCD camera after reconstruction with rapidSTORM (a) and a picture obtained through summing all recorded frames (b), equivalent to a widefield image. No drift correction was applied to the time-series. (Scalebar = $10 \mu m$)

2.2 Localization with post-processing

Especially in poor imaging condition, applying our learned black-box model described in section 1.3.1 turned out to be beneficial. Each frame using the trained network, before the processed image-stack is fed into the localization software.

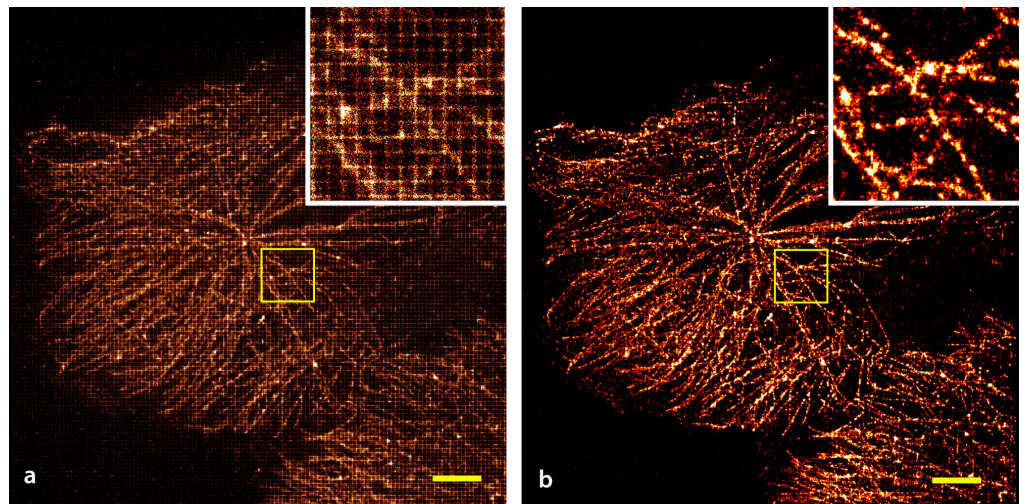


Figure 3. Comparison between unprocessed data and processed data. The neural network successfully got rid of the pattern effect which is due to the compression of the video stream. Scalebar = $1 \mu m$

Particularly at low-light conditions, SNR decreased dramatically. The low signal does not only suffer a reduced dynamic range, but even is clipped to zero below a minimum intensity by the sensor and preprocessing hardware. Furthermore the video-compression algorithm encodes a specific block structure into the data, where the hard edges are interpreted as blinking fluorophores by the localization software Fig. (3 a). Applying

our learned forward model reduces such artifacts significantly (Fig. 3b).

The NN was trained on a dataset consisting of frames from previously localized emitters from a noisy video-stream (see Supplement A.3) and artificially created blinking fluorophores processed by our simulated camera model (see Supplement A.1).

In cases, where the imaging conditions are good, the NN is not necessarily optimizing the result. This method is thus especially useful for the wide variety of cameras whose SNR is much worse or the sample preparation leads to low intensity in the *d*STORM experiment.

A next neighbor analysis of the ground truth data of a simulated STORM data-stack with non-processed and preprocessed simulated data stacks with compression artefacts are showing the strength of our NN approach. Especially out-of focus or by the compression artifact artificially created localization events were successfully eliminated. Hence the average localization accuracy (calculated as the mean deviation from the ground truth) was dramatically improved (see section B.2).

3 Discussion

We have demonstrated the suitability of using a modern smartphone camera for imaging beyond the diffraction limit. Even considering the limitations imposed by current smartphone hard- and software, i.e. low-light performance and artifacts caused by compression and image “enhancement” algorithms currently unavoidably being introduced by the camera chips, we have been able to resolve sub-diffraction detail in cytoskeletal structures on a level similar to conventional *d*STORM setups.

Preprocessing by a trained neural network albeit being useful in some cases has to be used with care, because one can hardly judge, what the network really learned. The localization uncertainty learned by misaligned data-pairs produces blurred results whose resolution is less than unprocessed data. Yet, it allowed a proof-of-concept recovery of the (d)STORM forward model for the smartphone sensor at poor imaging conditions. At the same time it may introduce additional localization uncertainties.

4 Conclusions

We showed that widely available cellphone cameras can be used for SMLM yielding image quality comparable to much more expensive professional cameras. This is a milestone in the development of an overall very cost-effective SMLM system. It also paves the way of making super-resolution microscopy widely available, which has the potential to accelerate scientific work. Specific neuronal processing units inside new cellphones makes it also very interesting to integrate the localization done by a NN inside the acquisition device, reducing the footprint of this technique significantly. Education also benefits from this approach directly, where ordinary cellphones are readily available. This removes barriers for future research of all levels of society and could bring new contributions to the field of biological and medical research.

5 Acknowledgments

We thank especially Ingo Fuchs who helped a lot in understanding the principles of the acquisition process of cellphone cameras. We also thank im for the support of the software design. Our project was funded by the DFG Transregio Project TRR166, TP04.

Supplementary Material

A Hardware Setup

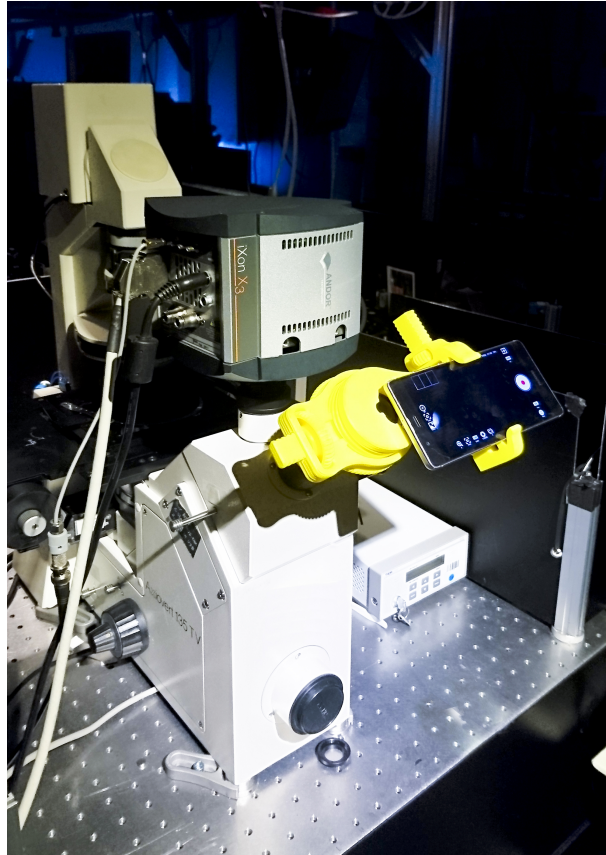


Figure 4. The custom made, 3D-printed cellphone adaptor in place on the Zeiss Axiovert microscope body

B Camera Characteristics

A characteristic mean-variance plot is generated for the HUAWEI P9 camera, from a set of unprocessed raw images aquired in snap-mode (12Bit DNG) of an intentionally defocussed but stationary object (see Fig. 5) by using the Dip-Image [53] "cal_readnoise" routine. It can be seen that the variance does not increase linearly with the mean intensity as it should for a shot-noise-limited sensor [54]. The noise parameters extracted from the low-intensity range of the curve are offset = 4,074 ADU; gain = 0,34 e/ADU; readnoise(Bg) = 1,23 e^- RMS; at an ISO3200, which was also used during our measurements.

Especially noteworthy is the low readnoise in Fig. 5. However, it cannot be guaranteed that the hardware-based preprocessing especially in the video-mode does not alter this value.

A series of images of dark background acquired in the video-mode with the HUAWEI P9, automatically compressed with a H264 encoder, shows another problematic property. The mean of each dark frame over time is shown in Fig. 6. It can be seen that the overall intensity is reduced over time. This might be a thermal problem, although the

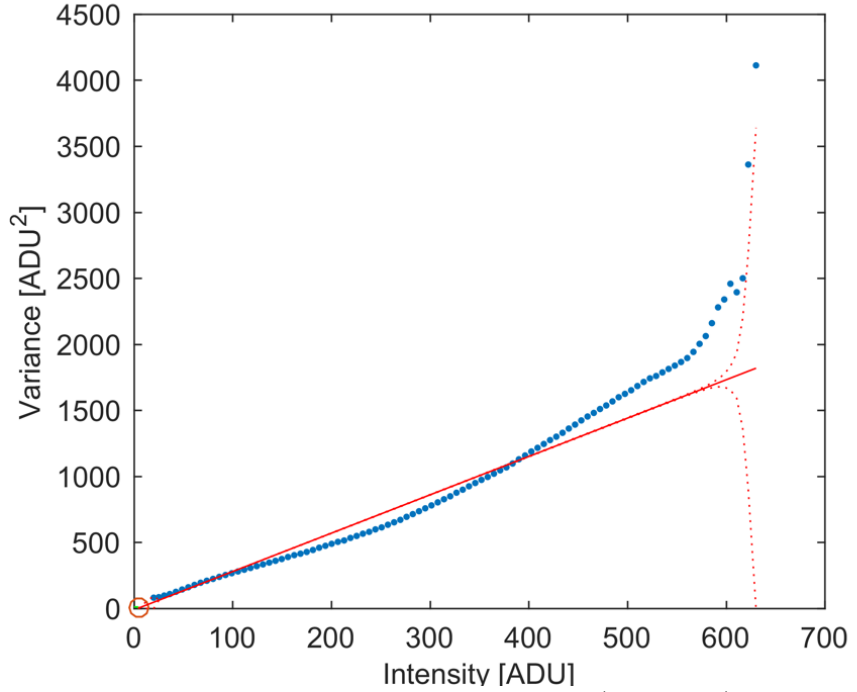


Figure 5. Mean-variance plot generated using a series (ISO=3200) of unprocessed raw images ("snap-mode") acquired by a HUAWEI P9 camera (blue points). The variance does not increase linear with the mean intensity (best fit in red), so that there must be additional noise sources in the images. Measured values for offset = 4,074 ADU; gain = 0,34 e/ADU; readnoise(Bg) = 1,23 e RMS; fixed pattern noise (BG) = 0.343 e RMS.

signal is expected to rise rather than drop. This effect, however, might also be caused by the compression of the incoming signal. Unfortunately the HUAWEI P9 has neither a temperature sensor on the chip nor a reproducible data compression, so that it stays unclear what the reason is. In addition, the signal drops periodically (every 1.07 s at 20 fps) which seems to be a compression artifact. A homogeneous although slightly noisy line would have been expected. The acquisition of a video shows already the drawback and limitations of the compression.

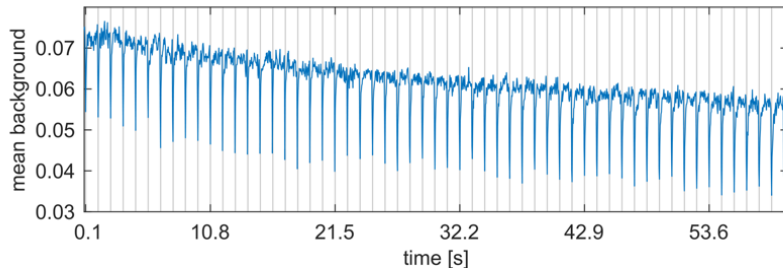


Figure 6. Mean of a dark image acquired with a HUAWEI P9 camera and compressed with a H264 encoder as a function over time. The overall decay of the signal and the periodic drop of the signal demonstrates the disadvantages of a compressed video signal. Equidistant gray lines (vertical) with 1.07 s spacing show the periodicity of the drop in the intensity signal.

Looking at Fig 6 it can be seen that the HUAWEI P9 sensor and video compression codec add a remarkable amount of noise to an image. Imaging techniques that require extensive image processing will have problems using such data. However, wide-field microscopy of bright specimens will be less affected. The localization accuracy of SMLM will be impaired the more noise each raw image contains. However noise alone will not create artifacts. The occurring drop of the overall intensity is no problem either, because each image is processed individually and offset variations are automatically accounted for by rapidSTORM and ThunderSTORM.

C Neural Network Architecture and Training

A Generation of the training dataset

Here we describe the generation of the dataset "A to B" to feed the modified version of the pix2pix generative adversary neuronal network detailed described in Supplement B. The idea is to recover B, i.e. adjusted for the effects of compression or noise, from a captured video-frame A by applying the trained network. We propose three different methods to produce suitable training sets.

A.1 Dataset from camera's model simulation

We first created a data-stack of simulated STORM frames using the software testSTORM [55]. Parameters of line- as well as randomly oriented vesicles structures were chosen according to our experimental conditions. In a later step we estimated a camera model, based on the properties determined in Supplement B, to introduce noise into the data, before they were compressed by the H.264 video-codec in MATLAB [56]. The compression ratio was tuned, so that the compression artifacts looked similar to the one from the original acquisition ("Video-Quality": 20%). Combining the decompressed simulated video-frames with the position of the ground truth events convolved with the system's PSF represent the dataset for training the NN.

Following this procedure gives only an estimated forward model of the unknown camera black-box and therefore most probably does not account for all properties of the data acquired by the cell-phone camera.

A.2 Dataset from imaged groundtruth data from a second display

To incorporate unknown influence of the camera's firmware, we created a dataset consisting of captured frames from ground truth data (see Supplement A.1). The time-series was played as a movie on a secondary LCD from another cellphone (Sony Xperia Z5, 1080p, IPS-LCD, Japan) and is recorded in the video-mode by the HUAWEI P9 at about 114 mm distance. Experimental parameters like exposure-time and sensitivity (ISO), as well as the expected PSF (point spread function) are chosen to correspond to the dSTORM experiments. To avoid a moiré-effect due to the pixelated structure of the ground-truth display, we slightly defocused the image on the HUAWEI P9. Inhomogeneities in the illumination were compensated by flat-fielding the images before they were fed to the NN for training.

To produce a matching dataset, where each camera frame corresponds to its equivalent ground-truth (GT) frame displayed on the secondary screen, we encoded a barcode representing the actual frame number of the ground truth data, into the displayed video. In a post-processing step, first the barcode is readout and assigned to the equivalent ground-truth frame number. To avoid any ambiguous overlap exposures between any two frames, we took only every 3rd frame after detecting a barcode. The framerate of

the GT-movie and acquisition device was set to have a correct sampling in time (e.g. four frames).

To account for misalignment between the two frames in the registration procedure, we first estimated the affine transformation parameters and later transformed the GT frames using the Dip-Image toolbox [53] for MATLAB [56] to have sub-pixel accurate registered images.

A.3 Dataset from localized dSTORM data

Due to barrel-like lens distortions, the frames in the previous method (section A.2) did not match over the entire field of view. Thus the NN learned a location invariant localization uncertainty. The U-NET [39] based generator of the GAN recovers the PSF at randomly shifted positions, based on the misaligned dataset in the range of about a quarter of a pixel. When localizing the processed image-series using ThunderSTORM the randomly varying shift of the PSF produces blurry results.

Therefore we created a third way to generate a dataset by taking captured *d*STORM time-series using the video-mode from real biological cells (labelled microtubules) under optimal conditions. After localizing the blinking events using ThunderSTORM for each frame, we extract the detected emitters and draw gaussian PSFs according to the fluorophore’s position on a bitmap image.

To not only learn the forward model from the ThunderSTORM PSF-fitting algorithm, we also incorporated data from the method described in Supplement A.1. This enhanced the quality after processing the frames and increases the number of correctly detected blinking events. It also successfully accounted for variations in sample’s background as well as in the camera parameters.

B Network Architecture

The registered (time/location) data-pairs feed our modified version of the image-to-image GAN network, which was implemented in the open-source ML library PyTorch [57]. The code is based on the open-sourced version described in [58].

To circumvent a checkerboard-like artifact in the reconstruction process, we replaced the deconvolution operation in the decoding step of the U-NET [39] generator by a resize-convolution layer as suggested in [59], based on the nearest-neighborhood interpolation method. This immediately eliminates the high-frequency patterns due to the low coverage of the convolutions in the deconvolution process.

The neural network (NN) was trained on a Nvidia Titan X GPU over 5000 frames with equal acquisition parameters like the one in the real *d*STORM experiment taken from method one (Supplement A.1) and three (Supplement A.3) to equal parts. We use minibatch SGD and relied on the ADAM optimization scheme with learning rate of $1E-4$ and momentum of $\beta = 0.25$. The number of first-layer filters in the PatchGAN-discriminator [60] and U-NET generator was chosen to be 32 each.

Compared to approaches like the recent published Deep-STORM by Nehme et al. [40], the here presented GAN does not require a particular cost-function which tries to produce optimal result with the generator. Instead the discriminator tries to distinguish whether the results are coming from the generator or provided by the GT data. Hence the GAN should come up with a learned forward model which successfully includes all unknown effects to map the acquired camera frames to images which then follow the forward model of the *d*STORM technique much better. This facilitates a parameter free optimization technique.

B.1 Training and Evaluating the Network

Our experiment showed, that the training converged to equilibrium after 100 epochs at a batchsize of 4 frames, which follows in about 2h time-effort on an ordinary desktop machine with 64Gb RAM, Intel Xeon octacore, and a Nvidia TitanX graphics card with 12GB memory. It is worth noting, that a precise alignment of the data is crucial, otherwise the recovered events will be shifted by an unknown amount and the localization fails due to smeared-out blinking events.

Applying the trained network takes about 5 Minutes for a stack of fifteen thousand frames of 256×256 pixels. Due to the convolutional-architecture of the PatchGAN it is possible to process data with framesizes different than the training dataset in case the pixel information in the radius of the convolutional kernel are uncorrelated i.e. following random Markovian fields [44, 61], which is the case for *d*STORM measurements. Our approach does not rely on any specific class of imaged objects, nor does it need any parameters other than a dataset which mimics the experimental data in the sense of acquisition parameters.

B.2 Quantitative Analysis of results using NN

To give a quantitative measure of how well the NN recovers data suffering from noise and compression artifacts we again simulate a STORM-dataset from the Leibniz-Institute’s logo (Fig. 7 b, c) using testSTORM based on our camera model proposed in B. We localize the events using ThunderSTORM and measure the distance between recovered blinking and ground-truth positions using MATLAB’s function ”knnsearch”.

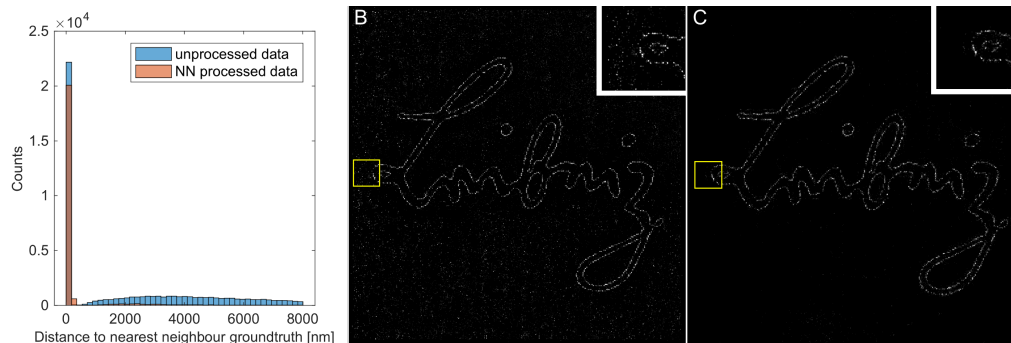


Figure 7. Histogram in a, where we compare the distance between the ground-truth positions and the detected localization from unprocessed and NN-processed data. From this and the reconstructed SMLM images in b (unprocessed data) and c (NN-processed data) it is clearly visible, that the NN successfully distinguish between true blinking events and detected events coming from noise- or compression artifacts. Number of detected events compared to ground-truth: 22658; unprocessed video: 50509; NN-processed video: 22658

Especially for experiments, where noise is dominant, the NN is capable to differentiate between false-positive and true blinking events. From the histogram in Fig. 7, giving the distances between nearest neighbors in GT and unprocessed as well as GT and NN-processed events for each frame, it is clearly visible, that the NN enhances the localization accuracy.

References

1. Betzig, E. *et al.* Imaging intracellular fluorescent proteins at nanometer resolution. *Science (New York, N.Y.)* **313**, 1642–5. ISSN: 1095-9203 (2006).
2. Hess, S. T., Girirajan, T. P. & Mason, M. D. Ultra-high resolution imaging by fluorescence photoactivation localization microscopy. *Biophysical Journal* **91**, 4258–4272. ISSN: 00063495 (2006).
3. Rust, M. J., Bates, M. & Zhuang, X. Sub-diffraction-limit imaging by stochastic optical reconstruction microscopy (STORM). *Nature Methods* **3**, 793–795. ISSN: 15487091 (2006).
4. Hell, S. W. & Wichmann, J. Breaking the diffraction resolution limit by stimulated emission: stimulated-emission-depletion fluorescence microscopy. *Optics Letters* **19**, 780. ISSN: 0146-9592 (1994).
5. Klar, T. A. & Hell, S. W. Subdiffraction resolution in far-field fluorescence microscopy. *Optics Letters* **24**, 954. ISSN: 0146-9592 (1999).
6. Heintzmann, R. & Huser, T. *Super-Resolution Structured Illumination Microscopy* Dec. 2017. doi:10.1021/acs.chemrev.7b00218. <<http://pubs.acs.org/doi/10.1021/acs.chemrev.7b00218>>.
7. Tolstik, E., Shukla, S. & Heintzmann, R. in *The Optics Encyclopedia* 1–31 (Wiley-VCH Verlag GmbH & Co. KGaA, Weinheim, Germany, June 2015). doi:10.1002/9783527600441.oe1007. <<http://doi.wiley.com/10.1002/9783527600441.oe1007>>.
8. Abbe, E. Beiträge zur Theorie des Mikroskops und der mikroskopischen Wahrnehmung. *Archiv für mikroskopische Anatomie* **9**, 413–418. ISSN: 0176-7364 (1873).
9. Saurabh, S., Maji, S. & Bruchez, M. P. Evaluation of sCMOS cameras for detection and localization of single Cy5 molecules. *Optics Express* **20**, 7338. ISSN: 1094-4087 (2012).
10. Diekmann, R. *et al.* Characterization of an industry- grade CMOS camera well suited for single molecule localization microscopy – high performance super-resolution at low cost. *Scientific Reports* **7**, 14425. ISSN: 2045-2322 (Dec. 2017).
11. Statista. • *Number of smartphone users worldwide 2014-2020* — Statista 2017. <<https://www.statista.com/statistics/330695/number-of-smartphone-users-worldwide/>> (2018).
12. DENDERE, R., Myburg, N. & Douglas, T. T. S. A review of cellphone microscopy for disease detection. *Journal of Microscopy* **260**, 248–259. ISSN: 13652818 (Dec. 2015).
13. Dong, S. *Developments of Gigapixel Microscopy* (2014).
14. Breslauer, D. N. *et al.* Cellscope: mobile microscopy for single cell analysis. *October*, 456–458 (2008).
15. Phillips, Z. F. *et al.* Multi-Contrast Imaging and Digital Refocusing on a Mobile Microscope with a Domed LED Array. *Plos One* **10** (ed Coles, J. A.) e0124938. ISSN: 1932-6203 (May 2015).
16. Rasooly, R. *et al.* Improving the Sensitivity and Functionality of Mobile Webcam-Based Fluorescence Detectors for Point-of-Care Diagnostics in Global Health. *Diagnostics* **6**, 19. ISSN: 2075-4418 (2016).
17. Diederich, B., Wartmann, R., Schadwinkel, H. & Heintzmann, R. Using Machine-Learning to Optimize phase contrast in a Low-Cost Cellphone Microscope. arXiv: 1712.06891. <<http://arxiv.org/abs/1712.06891>> (Dec. 2017).

-
18. Phillips, Z. *et al.* *Computational CellScope: Multi-Contrast Imaging on a Smartphone-Based Microscope Using a Domed Programmable LED Array* in *Optics in the Life Sciences* (2015), BM3A.7. ISBN: 978-1-55752-954-1. doi:10.1364/BODA.2015.BM3A.7. <<https://www.osapublishing.org/abstract.cfm?uri=BODA-2015-BM3A.7>>.
 19. Orth, A., Wilson, E. R., Thompson, J. G. & Gibson, B. C. A dual-mode mobile phone microscope using the onboard camera flash and ambient light. *Scientific Reports* **8**, 3298. ISSN: 2045-2322 (Dec. 2018).
 20. Ma, H., Fu, R., Xu, J. & Liu, Y. No Title. **7**, 1542. ISSN: 2045-2322 (2017).
 21. Holm, T. *et al.* A Blueprint for Cost-Efficient Localization Microscopy. *ChemPhysChem* **15**, 651–654. ISSN: 14394235 (2014).
 22. OpenOcular. *Smartphone to Optics Adapter V1* by OpenOcular - Thingiverse 2017. <<https://www.thingiverse.com/thing:2567141>> (2018).
 23. Inc., H. *HUAWEI P9 Debuts in London with Dual Camera Lens, Reinvents Smartphone Photography in Collaboration with Leica — HUAWEI Latest News — HUAWEI Global* <<https://consumer.huawei.com/en/press/news/2016/hw-474971/>> (2018).
 24. Galstian, T. *Smart mini-cameras* 323. ISBN: 9781466512924 (2006).
 25. Nakamura, J. IMAGE SENSORS and SIGNAL PROCESSING for DIGITAL STILL CAMERAS. <<http://last.hit.bme.hu/download/firtha/video/Sensors/Junichi%20Nakamura%20Image%20sensors%20and%20signal%20processing%20for%20digital%20still%20cameras%202006.pdf>>.
 26. Qualcomm Technologies, I. & Qualcomm. *Whitepaper: Breakthrough mobile imaging experiences* tech. rep. (2014).
 27. Sony Cooperation, J. *Datasheet Sony IMX214-0AQH5-C* tech. rep. (Japan, 2014), 1–48.
 28. Omnivision. 12-Megapixel PureCel[®] Plus Sensors for Dual and Single Cameras in Mobile Applications OV12A10-OV12A1B (2017).
 29. Brian Klug. *Talk: Understanding Camera Optics & Smartphone Camera Trends, A Presentation by Brian Klug* 2013. <<https://www.anandtech.com/show/6777/understanding-camera-optics-smartphone-camera-trends>> (2018).
 30. Google Inc. *Developer Reference: android.hardware.camera2* 2015. <<https://developer.android.com/reference/android/hardware/camera2/package-summary.html>> (2018).
 31. Smith, Z. J. *et al.* No Title. **6** (ed Rubinsky, B.) e17150. ISSN: 1932-6203 (Mar. 2011).
 32. Skandarajah, A., Reber, C. D., Switz, N. A. & Fletcher, D. A. Quantitative imaging with a mobile phone microscope. *PLoS ONE* **9**, e96906. ISSN: 19326203 (2014).
 33. Sung, Y., Campa, F. & Shih, W.-C. Open-source do-it-yourself multi-color fluorescence smartphone microscopy. *Biomedical Optics Express* **8**, 5075. ISSN: 2156-7085 (Nov. 2017).
 34. Fuchs, I. *Github: FreedCam* 2018. <<https://github.com/KillerInk/FreeDcam>>.
 35. Diederich, B. & Fuchs, I. *Github: cellSTORM Android APP* 2018. <<https://github.com/bionanoimaging/cellSTORM-ANDROID>>.
 36. ITU-T. H.264. *International Telecommunication Union* (2013).

-
37. Wiegand, T., Sullivan, G., Bjontegaard, G. & Luthra, A. Overview of the H.264/AVC video coding standard. *IEEE Transactions on Circuits and Systems for Video Technology* **13**, 560–576. ISSN: 1051-8215 (2003).
 38. Çiçek, Ö., Abdulkadir, A., Lienkamp, S. S., Brox, T. & Ronneberger, O. *3D U-net: Learning dense volumetric segmentation from sparse annotation* in *Lecture Notes in Computer Science (including subseries Lecture Notes in Artificial Intelligence and Lecture Notes in Bioinformatics)* **9901 LNCS** (2016), 424–432. ISBN: 9783319467221. doi:10.1007/978-3-319-46723-8_49. arXiv: 1606.06650.
 39. Ronneberger, O., Fischer, P. & Brox, T. U-Net: Convolutional Networks for Biomedical Image Segmentation. *Miccai*, 234–241. ISSN: 16113349 (2015).
 40. Nehme, E., Weiss, L. E., Michaeli, T. & Shechtman, Y. Deep-STORM: Super Resolution Single Molecule Microscopy by Deep Learning. arXiv: 1801.09631. <<http://arxiv.org/abs/1801.09631>> (Jan. 2018).
 41. Creswell, A. *et al.* Generative Adversarial Networks: An Overview. <<https://arxiv.org/pdf/1710.07035.pdf>>.
 42. Glasner, D., Bagon, S. & Irani, M. *Super-resolution from a single image* in *Proceedings of the IEEE International Conference on Computer Vision* (2009), 349–356. ISBN: 9781424444205. doi:10.1109/ICCV.2009.5459271. arXiv: 1505.0729.
 43. Sinha, A., Lee, J., Li, S. & Barbastathis, G. Lensless computational imaging through deep learning. *Optica* **4**, 1117. ISSN: 2334-2536 (2017).
 44. Isola, P., Zhu, J.-Y., Zhou, T. & Efros, A. A. Image-to-Image Translation with Conditional Adversarial Networks. arXiv: 1611.07004. <<http://arxiv.org/abs/1611.07004>><<https://arxiv.org/abs/1611.07004>> (Nov. 2016).
 45. Johnson, J., Alahi, A. & Fei-Fei, L. *Perceptual losses for real-time style transfer and super-resolution* in *Lecture Notes in Computer Science (including subseries Lecture Notes in Artificial Intelligence and Lecture Notes in Bioinformatics)* **9906 LNCS** (2016), 694–711. ISBN: 9783319464749. doi:10.1007/978-3-319-46475-6_43. arXiv: 1603.08155.
 46. Wang, C. *et al.* Discriminative Region Proposal Adversarial Networks for High-Quality Image-to-Image Translation. <<https://arxiv.org/pdf/1711.09554.pdf>> (2017).
 47. Goodfellow, I. *et al.* Generative Adversarial Nets. *Advances in Neural Information Processing Systems 27*, 2672–2680. ISSN: 10495258 (2014).
 48. Boyd, N., Jonas, E., Babcock, H. P. & Recht, B. DeepLoco: Fast 3D Localization Microscopy Using Neural Networks. *bioRxiv*, 267096 (Feb. 2018).
 49. Whelan, D. R. & Bell, T. D. Image artifacts in single molecule localization microscopy: Why optimization of sample preparation protocols matters. *Scientific Reports* **5**. ISSN: 20452322. doi:10.1038/srep07924 (2015).
 50. Wolter, S. *et al.* rapidSTORM: accurate, fast open-source software for localization microscopy. *Nature Methods* **9**, 1040–1041. ISSN: 1548-7091 (Nov. 2012).
 51. Ovesný, M., Křížek, P., Borkovec, J., Švindrych, Z. & Hagen, G. M. ThunderSTORM: a comprehensive ImageJ plug-in for PALM and STORM data analysis and super-resolution imaging. *Bioinformatics* **30**, 2389–2390. ISSN: 1367-4803 (Aug. 2014).
 52. Banterle, N., Bui, K. H., Lemke, E. A. & Beck, M. Fourier ring correlation as a resolution criterion for super-resolution microscopy. *Journal of Structural Biology* **183**, 363–367. ISSN: 10478477 (2013).

-
53. Prof.Dr. Bernd Rieger, C. L. *DIPimage DIPlib 2.7.9* 2018. <<http://www.diplib.org/main>> (2018).
 54. Stijns, E. & Thienpont, H. in *Optical and Digital Image Processing: Fundamentals and Applications* 25–48 (2011). ISBN: 9783527409563. doi:10.1002/9783527635245.ch2. arXiv: 0408133v1 [arXiv:cond-mat].
 55. Novák, T., Gajdos, T., Sinkó, J., Szabó, G. & Erdélyi, M. TestSTORM: Versatile simulator software for multimodal super-resolution localization fluorescence microscopy. *Scientific reports* **7**, 951. ISSN: 2045-2322 (Apr. 2017).
 56. The MathWorks, Inc., N. *MATLAB* Massachusetts, United States., 2018.
 57. Paszke, A. *et al.* Automatic differentiation in PyTorch. *Advances in Neural Information Processing Systems* **30**, 1–4 (2017).
 58. Zhu, J.-Y. *CycleGAN and pix2pix in PyTorch* 2018. <<https://github.com/junyanz/pytorch-CycleGAN-and-pix2pix>>.
 59. Odena, A., Dumoulin, V. & Olah, C. Deconvolution and Checkerboard Artifacts. *Distill* **1**, e3. ISSN: 2476-0757 (Oct. 2016).
 60. Hou, L. *et al.* Patch-based Convolutional Neural Network for Whole Slide Tissue Image Classification. arXiv: 1504.07947. <<http://arxiv.org/abs/1504.07947>> (Apr. 2015).
 61. Li, C. & Wand, M. Precomputed Real-Time Texture Synthesis with Markovian Generative Adversarial Networks. arXiv: 1604.04382. <<http://arxiv.org/abs/1604.04382>> (Apr. 2016).

cellSTORM – cost-effective super-resolution on a cellphone using dSTORM

Benedict Diederich^{1,2,*}, Patrick Then^{1,2}, Alexander Jügler^{1,2}, Ronny Förster^{1,2}, Rainer Heintzmann^{1,2}

¹ Leibniz Institute of Photonic Technology, Albert-Einstein Str. 9, 07745 Jena, Germany

² Institute of Physical Chemistry and Abbe Center of Photonics, Friedrich-Schiller-University Jena, Helmholtzweg 4, 07743 Jena, Germany

* benedict.diederich@ipht-jena.de

Abstract

Expensive scientific camera hardware is amongst the main cost factors in modern, high-performance microscopes. Recent technological advantages have, however, yielded consumer-grade camera devices that can provide surprisingly good performance. The camera sensors of smartphones in particular have benefited of this development. Combined with computing power and due to their ubiquity, smartphones provide a fantastic opportunity for "imaging on a budget". Here we show that a consumer cellphone is capable even of optical super-resolution imaging by (direct) Stochastic Optical Reconstruction Microscopy (*d*STORM), achieving optical resolution better than 80 nm. In addition to the use of standard reconstruction algorithms, we investigated an approach by a trained image-to-image generative adversarial network (GAN). This not only serves as a versatile technique to reconstruct video sequences under conditions where traditional algorithms provide sub-optimal localization performance, but also allows processing directly on the smartphone. We believe that "*cell*STORM" paves the way for affordable super-resolution microscopy suitable for research and education, expanding access to cutting edge research to a large community.

Introduction

Super-resolution by Single Molecule Localization Microscopy (SMLM) techniques like Photo-Activated Localization Microscopy (PALM) [Betzig2006, Hess2006] or (direct) Stochastic Optical Reconstruction Microscopy (*d*STORM) [Rust2006] is well established in biology and medical research. Together with other modalities like Stimulated Emission Depletion (STED) [Hell1994, Klar1999] and Structured

Illumination Microscopy (SIM) [Heintzmann2017, Tolstik2015], SMLM revolutionized optical far-field microscopy beyond the Abbe limit [Abbe1873].

Typically these methods rely on costly hardware for excitation and detection [Saurabh2012, Diekmann]. Scientific grade sCMOS or emCCD cameras are a major cost factor, as high photon efficiency and low noise are paramount. However, successful attempts to image single molecules using low-cost CMOS cameras to build cost-effective SMLM setups for educational environments [Ma2017, Holm2014, Diekmann] demonstrate that the imaging quality of such sensors suffices for SMLM. Furthermore, the evolution of mobile phones created surprisingly powerful cameras and sensors worth considering as an alternative. Almost 2.3 billion smartphones are actively in use [Statista2017]. This causes a widespread availability of high quality cameras backed by respectable computational power. All that is available at a very low price, where each development iteration aims to further optimize not only the image quality, but also the general performance of the handheld devices [Dendere2015].

This gave rise to the developing field of mobile microscopy, which so far resulted in hand-held devices capable of quantitative phase-imaging of biological material by combining the cellphone with customized hardware adapters [Dong2014, Phillips2015a] or act as portable diagnosis devices to detect e.g. water-borne parasites [Phillips2015a, Diederich2017c, Orth2018]. This makes smartphones suitable not only for educational environments, but also for rapid-prototyping applications, where the processing can be done on the cellphone itself to keep size and costs small.

Common smartphone camera sensors are equipped with Bayer patterned filters, significantly lowering the detection efficiency compared to monochromatic imaging. Recently, some new camera modules, as in the Huawei® P9, feature sensitive monochromatic CMOS camera chips. However, acquiring high quality RAW data using a cellphone is nevertheless very challenging. Hardware abstraction layers embedded into the firmware of the camera module prevent accessing the raw pixel values. Compression and noise artifacts are therefore a potential problem of imaging with smartphone cameras.

We show that by simple adaption of the mobile phone device to a common widefield microscope equipped with an excitation laser it is possible to image well below the diffraction limit. Additionally we present a novel machine-learning-based image processing algorithms being able to process *d*STORM experiments directly on the device.

1 Results

1.1 Cellphone data acquisition

In order to image the blinking fluorophores, we attached the smartphone (P9 EVA-L09, Huawei ®, China, Table 1) directly to the eyepiece of a standard inverted research microscope (AxioVert 135 TV, Zeiss, Germany) with a 3D-printed interface. For all experiments we use a 12 Bit monochromatic sensor chip (Sony IMX 286, Japan, Table 1, [Inc.b]) of the P9’s dual-camera module. The aim of the camera manufacturer is to ensure optimal image quality in everyday environments. Tailored algorithms help to hide problems introduced e.g. by the small pixels and lens dimensions [Galstian, Nakamura].

In contrast to industry-grade CMOS cameras, the acquired images of cellphone cameras are post-processed by proprietary firmware, called the image signal processor (ISP) [QualcommTechnologies2014, Ova]. This allows real-time optimization of the image quality. It is mainly responsible for demosaicing the Bayer-pattern to generate RGB images, but also reduces the effect of lens aberrations and removes hot-pixels or thermal noise [BrianKlug2013, Galstian]. Additionally it provides hardware control (e.g. autofocus, optical image stabilization) and encodes the video-stream into less memory-consuming formats.

Modern cellphones offer the raw camera sensor pixel values (*“snap-mode”*), i.e. the sensor data before further processing or compression by e.g. JPEG/MPEG algorithms [Diederich2017c, Smith2011b, Skandarajah2014a, Sung2017]. However, *d*STORM requires continuous and fast acquisition over several minutes to record sufficient fluorescence events for image reconstruction, which is incompatible with snap-mode acquisition. The computational effort to save a time-series of raw-frames makes it impracticable for these measurements. Hence, we were forced to use the standard time-series acquisition mode (*“video-mode”*), where the compression of the raw data was unavoidable.

Acquiring monochromatic video-sequences is not part of the cellphone’s software. We thus wrote a customized application (APP) based on the open-sourced camera library *“FreeDcam”* [Fuchs2018, Diederich2018], which enables the full control over the camera parameter like sensitivity (ISO), focus position, exposure time and frame-rate, as well as the access to the monochromatic chip.

Down-converting the video-stream, e.g. using the H264 video-codec, is also implemented on the ISP. To reduce the amount of memory, it relies on the exact-match integer transform [Wiegand2003] which uses reference images and calculates residual/difference images to reduce the amount of redundant information. This lossy compression partly obscures accurate information of the pixel, necessary for precise localization of the fluorophores.

1.2 Localization based on Machine Learning Algorithms

In general, machine learning (ML) has the ability to create an implicit model which maps a set of input variables onto a set of outputs [Cicek2016, Ronneberger2015, Nehme2018, Creswell]. A large variety of different network architectures applied to image processing problems have shown that using prior knowledge, single-image super-sampling [Glasner2009] or recovering the optical phase from an intensity image [Sinha2017] is possible.

Motivated by recent approaches where an adversarial network architectures (GAN) [Goodfellow2014] was trained on a noise model [Creswell] or the variational auto-encoder-based neural network (VAE) which directly localize STORM events [Nehme2018], we propose a localization algorithm which accounts for strongly compressed noisy data (see Methods C). Compared to the VAE, the GAN architecture of the NN has the ability to be used more generically. We found that, once trained, it serves as a parameter-free localization method for multi-emitter fitting in compressed image-streams as well as image sequences coming from an emCCD camera chip with different SNR ratios.

Following a modified version of the popular image-to-image GAN (Pix2Pix) [Isola2016b] network architecture (see Methods D and Fig. 1 a.) the goal of our network is to detect the origin (e.g. center position) as a pixel on a supersampled grid of a blinking fluorophore in a degraded video-frame of *cell*STORM measurements (referred to "x") and draw it on the appropriate position in the recovered frame (referred to "y").

Compared to conventional approaches, based on encoder-decoder networks [Johnson2016], the cost-function for the training process is not defined a priori but trained alongside the generator. This learned cost-function often fits the model better and avoids unwanted blurring of the results as often caused by using the L2-norm during training [Isola2016b, Wang].

Standard localization software like ThunderSTORM [Ovesny2014] applied to H.264-compressed noisy data produces many false localizations (indicated as blue markers in Fig. 1 d,e), whereas the trained NN successfully filters them (indicated as red markers in Fig. 1 d,e). The network's output is a table with the pixel-coordinates of local maxima of all localized events and a summation of all processed frames to produce a super-resolved image.

To ensure fast convergence of the network, we added prior information to the loss-function, which emphasize sparsity of the localized events. The adversarial loss is further able to interpret emitters where traditional algorithms provide suboptimal localization performance.

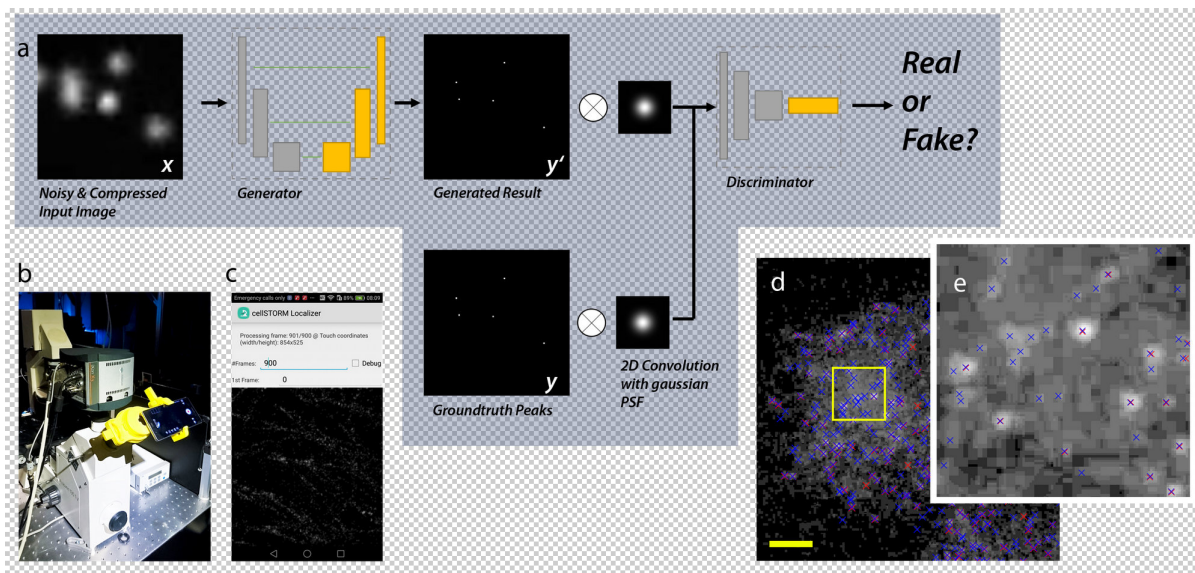


Figure 1. Architecture and Results from the GAN In (a) the image-to-image GAN architecture tries to find a generator-model which maps compressed and noisy input images to a localized version of the PSF’s origin. Image (d zoomed in e) shows a sample-frame (log-scale) from real *d*STORM measurements localized with ThunderSTORM (blue) and the NN (red). The number of falsely detected emitters is significantly lower in data processed by the NN. (b) shows the custom made, 3D-printed cellphone adapter attached to the Zeiss Axiovert microscope body holding the HUAWEI P9 running the cellSTORM Localizer APP shown in (c)

Our training datasets relies on mixed simulated as well as experimental data (further details in Methods D.1 and D.2). We create a ground truth (GT) stack of randomly blinking events with known positions y in ThunderSTORM, where noise based on our camera model (Methods C) and video-compression was added to simulate realistic camera frames x . Experimental data was produced by localizing an image-sequence of *cell*STORM measurements with ThunderSTORM and produce image-pairs with the detected origin of the molecules rendered as single pixel events y and their corresponding measured frame x . Mixing the datasets enables to learn a generic representation of the data and makes it possible to outperform ThunderSTORM’s [Ovesny2014] price-winning localization algorithm [Sage2015] in terms of localization-accuracy at low light conditions (Sec. 1.4).

For all results shown here we used the same trained NN.

Finally, since Tensorflow [Abadi] allows exporting and executing the trained networks to e.g. cell-phones, we wrote a custom APP [Diederichb] based on Tensorflow and OpenCV [3.0] which directly localizes a recorded video-stream on the device. This makes additional computational hardware redundant and promotes the cost-effective realization of super-resolution measurements to a greater extent. So far it poses as a proof-of-principle implementation, able to process 2 frames-per-second (frame-size of cropped

region: 64×64 pixels) on the Huawei® P9. Potentially, this could be significantly sped-up with new cellphone hardware (containing e.g. so-called Neuron Processing Units, or NPUs) or hardware accelerated implementation (e.g. Android Renderscript, Java Native Interface).

1.3 Localization-Results of Compressed Smartphone Data using Standard and Machine Learning Algorithms

The reduced SNR (signal-to-noise ratio) and blocking artifacts from video compression are directly apparent in the image sequences acquired by a cellphone camera (Fig. 1 d). Nevertheless, the robust nature of the reconstruction algorithms in rapidSTORM [Wolter2012] and ThunderSTORM [Ovesny2014] enables successful localization of blinking events even under non-ideal conditions. Both softwares yielded comparable results when reconstructing the final image from recorded data. The output was also used to verify our NN’s result to demonstrate the correct functionality.

Figure 2 shows the results obtained with *cellSTORM* from HeLa cells stained for tubulin using AlexaFluor 647-labeled primary/secondary antibodies. Applying both methods, NN-based localization (Fig. 2 d) and ThunderSTORM (Fig. 2 e) directly to the approximately 6 thousand acquired video images (at 20 fps), resolve the structure of microtubuli at a resolution of 75 nm measured using the Fourier ring correlation [Banterle2013]. To compare to conventional *dSTORM* data, we recorded another series of a similar cell using the emCCD camera of our setup. Due to the low photon yield at the cellphone camera, we opted against using a beamsplitter to simultaneously record the same area with the cellphone and the emCCD camera and instead imaged separate cells of the same sample.

The images acquired using the professional emCCD camera under identical buffer and illumination conditions (see Methods B) yielded a final resolution of 45 nm. While this number is smaller than for *cellSTORM* the relative difference is nonetheless surprisingly small.

1.4 Analysis of the NN-based localization approach

Especially under poor imaging conditions, applying our learned black-box model described in section 1.2 turned out to be beneficial. In several attempts to reconstruct the recorded video-stream using ThunderSTORM, we observed a grid-like pattern in the localized result (Fig. 4 a) which is likely due to the 4×4 block exact match integer-transform of the H.264 codec. It introduces abrupt changes in the local intensity, causing the localization algorithms to wrongly identify an event. Particularly at low-light

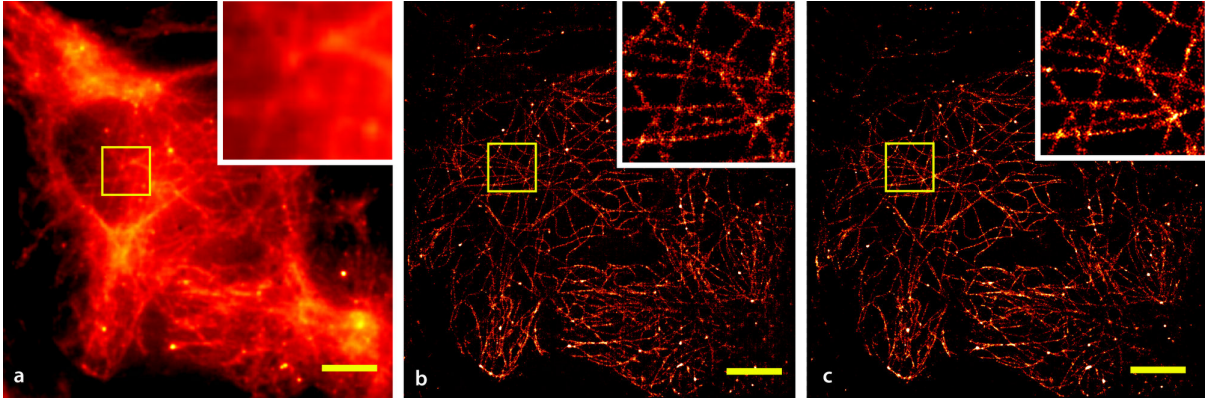


Figure 2. Comparison of cellSTORM results using NN and ThunderSTORM Microtubuli in HeLa cells stained using AlexaFluor 647 labeled antibodies and recorded with the cellphone camera. (a) a widefield equivalent image obtained by summing over all recorded frames, (b) the reconstructed result based on summing the NN-processed frames and (c) the output of the localization software ThunderSTORM using optimal parameters (no drift correction). (Scalebar = $3 \mu m$, $3\times$ Zoom in the yellow-boxed ROI)

conditions, the SNR decreased dramatically, further emphasizing this effect (Fig. 1 d/e, blue markers). In contrast, our NN-based approach reduced such artifacts significantly by filtering false-positive events (Fig. 1 d/e, red markers) and the final result in Fig. 4b).

To afford a quantitative comparison of how well the NN and ThunderSTORM recover data suffering from noise and compression artifacts, we measured the mean euclidean distance between all detected events and their corresponding ground truth events for every frame. An artificial STORM dataset of the Leibniz-IPHT institute’s logo and other test structures was generated in ThunderSTORM (Fig. 3 a). The stack (2000 frames, emitter density of $6/\mu m^2$, Fig. 3 b)) was processed by our camera model (Methods C) with varying compression quality (70%, 80%, 90%, 100%) to simulate different compressions that may occur in other smartphones. The number of photons per emitter (50, 100, 500, 1000) is also varied to demonstrate the functionality even below the normal achievable range of common fluorophores in Alexa647 (≥ 500 detected photons/fluorophore [Dempsey2011]). We processed all frames in ThunderSTORM using the same set of parameters (i.e. optimal result also for low SNR) to mimic the parameter-free localization procedure compared to the NN.

From the results in Fig. 4 it is clearly visible that the NN outperforms ThunderSTORM in terms of number of correctly detected events (only considering GT-neighbors closer than 200 nm) in all measurements. It also yields better accuracy in situations with more photons per emitter.

Nevertheless the accuracy degrades in low-light situations ($\leq 500 \frac{photons}{emitter}$) where ThunderSTORM

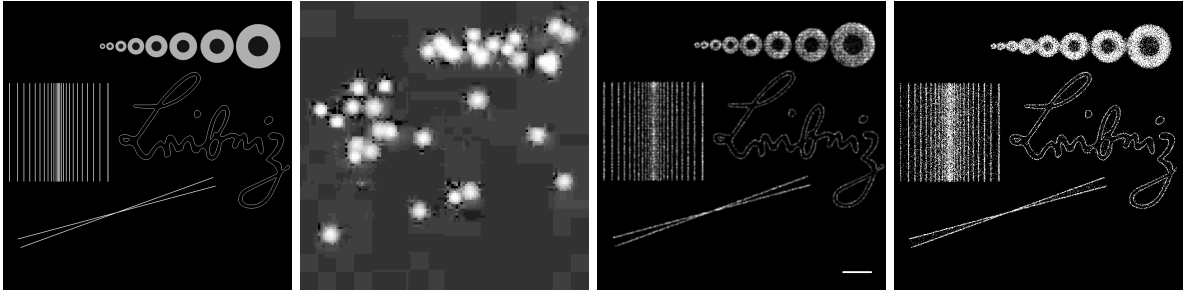


Figure 3. Qualitative Analysis of cellSTORM STORM-datasets created with ThunderSTORM. a) Ground truth of created test-target which is the basis for the generated STORM datasets with different H.264-compression rates and number of photons. b) Individual frame of the generated STORM-dataset with compression artefacts (1000 photons/fluorophores; compression ratio: 70%; resized, nearest-neighbors: 6 \times ; log-scale), Reconstructed image with our NN c) and ThunderSTORM d) (Scale bar: 1 μm)

achieves better localization accuracies at a price of less localized events. Here the NN exhibits around 20% more correctly detected events (blue bars in Fig. 3) at the expense of slightly reduced accuracy. This effect worsens at higher compression ratios.

Although the NN was not explicitly trained on a specific SNR-/compression-ratio, the improved results in the reconstruction above 500 $\frac{\text{photons}}{\text{emitter}}$ can be due to the composition of the training data. Besides simulated data it also contains experimental measurements from samples stained with Alexa647, typically emitting $\geq 500 \frac{\text{photons}}{\text{emitter}}$. This potentially indicates better results in this area and suggests that the NN can behave even better with tailored training-datasets in terms of expected photon statistics. However this goes along with reduced generality.

2 Discussion

We have demonstrated the suitability of using a modern smartphone camera for imaging beyond the diffraction limit. So far, unavoidable limitations imposed by current smartphone hard- and software, i.e. low-light performance and artifacts caused by compression and image “enhancement” algorithms, prevented the use for high-quality imaging. Nevertheless we have been able to resolve sub-diffraction detail in cytoskeletal structures on a level similar to conventional *d*STORM setups.

The nearest neighbor analysis of the ground truth data of a simulated STORM data-stack localized with ThunderSTORM and the NN are showing the strength of our NN approach. Out-of-focus or artifact affected localization events were successfully suppressed. Especially for photon statistics where we also used data from *cell*STORM experiments, the NN approach clearly outperformed ThunderSTORM in

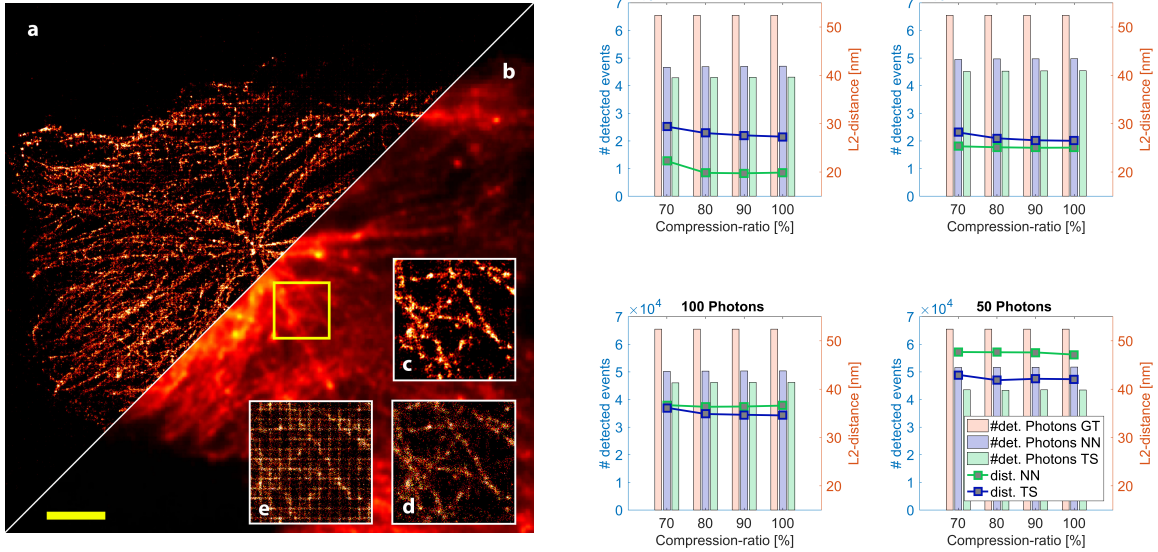


Figure 4. Quantitative and Qualitative Analysis of cellSTORM Results after summing all frames processed by the NN a) and directly coming from the camera b). When processing the video-sequence in ThunderSTORM, it introduces a checkerboard-like pattern shown in the twofold zoomed version of the yellow box in e), which can be reduced by adjusting the peak intensity threshold (e.g. $3 \cdot std(frame)$) illustrated in d). c) shows the NN’s result successfully compensating for the pattern effect, due to high noise and compression of the video stream. Scalebar = $5 \mu m$. The graphs on the right hand side visualize a comparison of the achieved localization accuracies of our NN and ThunderSTORM applied to simulated data. We varied the number of photons per emitter (1000, 500, 100, 50) as well as the compression ratio of the H.264 codec (70-100%), before the video-stream was localized by the NN and ThunderSTORM. We estimated the accuracy by measuring the Euclidean distance between a nearest neighbor in a GT and reconstructed frame and calculate the mean over all distances, visualized as green (NN) and blue (ThunderSTORM) plots. The green (NN) and blue (ThunderSTORM) bars indicate the number of correctly detected emitters within the allowed range of 200 nm compared to the 65.489 GT events (orange). It can be seen, that the NN always detects more good quality emitters, but with a loss of accuracy at lower intensities (i.e. $\leq 500 \frac{photons}{emitter}$) compared to ThunderSTORM.

terms of detected localizations and average localization accuracies (calculated as the mean deviation from the ground truth). This means our NN has the potential to perform even better in explicitly trained (real world) conditions and to easily customize the localization for each experiment individually.

The trained NN proved to be a robust and generic way to reconstruct *d*STORM data acquired by a smartphone sensor at poor imaging conditions, with sometimes a small loss of localization uncertainty. Additionally it serves as a blue-print for rapid software prototyping on mobile devices as the steps of computational expensive (pre-)processing as well as exhaustive debugging are carried out on desktop machines. The result can then easily be implemented on e.g. modern cellphones enabling e.g. diagnostics

or telemedicine in the field.

3 Conclusions

We showed that widely available cellphone cameras can be used for SMLM, yielding image quality approaching the performance of much more expensive professional cameras. This is a milestone in the development of an overall cost-effective SMLM system. It also paves the way of making super-resolution microscopy widely available, which has the potential to accelerate scientific work.

Specific NPU inside new cellphones further accelerates the convolutional processing of the data, which makes on-device reconstruction attractive. This not only reduces the system's complexity and footprint, but dramatically lowers the costs.

Educational environments, where ordinary cellphones are readily available, directly benefit from this approach. This removes barriers for future research of all levels of society and could bring new contributions to the field of biological and medical research.

4 Acknowledgments

We thank especially Ingo Fuchs who helped a lot in understanding the principles of the acquisition process of cellphone cameras as well as his support of the software design. We acknowledge funding by the DFG Transregio Project TRR166, TP04.

Methods

A Optical Setup

The basic *d*STORM-system is realized with a standard inverted microscope stand (AxioVert 135 TV, Zeiss, Germany) equipped with a nosepiece-stage (IX2-NPS, Olympus, Japan) to keep drift low. A 637 nm diode laser (P=150 mW, OBIS, Coherent, USA) is focused to the back-focal plane of the microscope objective lens (ZEISS 100 \times , NA=1.46) to realize a homogenous illumination in the sample plane. Using an adjustable mirror, it is also possible to change the laser position in the back-focal plane. This enables background-free total internal reflection (TIRF) illumination.

An emCCD camera (iXon3 DU-897, Andor, UK, Table 1) can be used to image the sample in widefield and STORM-mode during normal operation (*d*STORM reconstruction result Fig. 5). For imaging via the cellphone, the beam-path is switched from the camera port to the eyepiece, where a common 10 \times monocular eyepiece is equipped with a custom-made 3D-printed cellphone adapter [**OpenOcular2017**]. The cellphone (P9 EVA-L09, Huawei $\text{\textcircled{R}}$, China, Table 1) is placed with its camera lens in the Ramsden disk of the eyepiece (see Fig 1 b), since an eyepiece images the intermediate image produced by the tube lens of the Axiovert body to infinity.

Table 1. Comparison of a scientific-grade with a low-cost cell phone camera

	Andor iXonEM+ 897	Huawei$\text{\textcircled{R}}$ P9 (EVA-L09, Sony IMX286, Grayscale)
Pixel#:	512 \times 512	3980 \times 2460
Sensortype	(back-illuminated) emCCD	(back-illuminated) CMOS
Pixelsize (μm):	16	1,25
Bitdepth:	14 Bit	12 Bit
Read Noise (e^-):	0,2 RMS	1,23 RMS (see Methods C)
Quantum-Efficiency	$\geq 90\%$	$\approx 70 - 80\%$
Price	$\approx 20 \text{ k}\$$	$\approx 300 \text{ \$}$ (camera module: $\approx 20 \text{ \$}$)

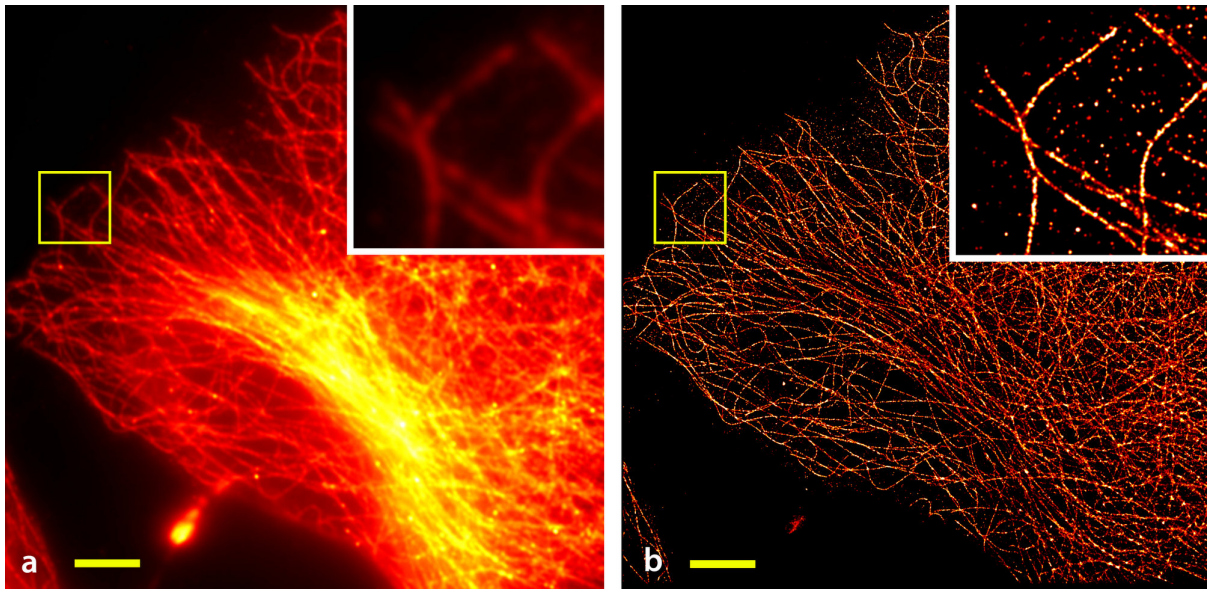


Figure 5. Result from the emCCD camera A widefield equivalent image obtained by summing over all recorded images from microtubuli in HeLa cells stained using AlexaFluor 647 labeled antibodies recorded with the Andor emCCD camera (a) and the image after reconstruction with rapidSTORM. No drift correction was applied to the time-series. (Scalebar = $6\ \mu\text{m}$, $3\times$ Zoom in the yellow-boxed ROI)

B dSTORM Imaging Samples and Results from an emCCD Camera

HeLa cell samples have been prepared using the PFA-fixation protocol outlined in [Whelan2015]. Microtubuli have been stained using monoclonal mouse anti- β -tubulin (Sigma Aldrich) and goat anti-mouse IgG secondary antibody (ThermoFisher Scientific), labeled with Alexa Fluor 647 at 1:150 and 1:300 dilution, respectively. All imaging experiments have been conducted in imaging buffer prepared freshly from 150-200mM MEA (β -Mercapto-ethylamine hydrochloride) in PBS and pH adjusted to 7.4 using NaOH. The oxygen scavenging effect from MEA has been proven efficient enough to refrain from additional enzyme-based oxygen scavenger systems.

C Camera Characteristics

A characteristic mean-variance plot is generated for the Huawei® P9 camera, from a set of 10 unprocessed raw images (snap-mode) acquired in 12Bit (DNG) of an intentionally defocussed but stationary object (see Fig. 6) by using the Dip-Image [Prof.Dr.BerndRieger2018] "cal_readnoise" routine.

It can be seen that the variance does not increase linearly with the mean intensity as it should for a shot-noise-limited sensor [Stijns2011]. The slope of the curve is the gain, which is constant up to an intensity of around 220 ADU. The noise parameters extracted from the linear low-intensity range of the curve are: offset = 4,1 ADU; gain = 0,69 e^- /ADU; readnoise(Bg) = 2,5 e^- RMS; at an ISO3200, which was also used during our measurements. In order to have a linear gain, the camera should not be exposed to much, so that the pixel values do not exceed the critical intensity value of 220 ADU.

Especially noteworthy is the low readnoise. However, it cannot be guaranteed that the hardware-based preprocessing especially in the video-mode does not alter this value.

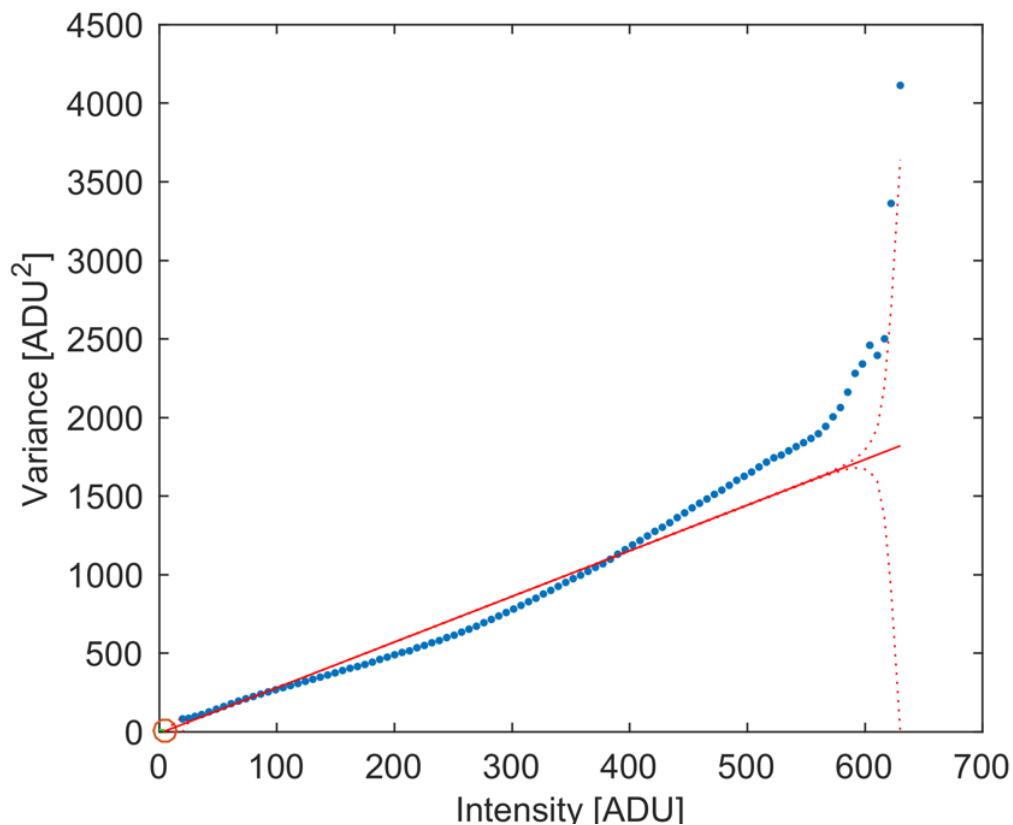


Figure 6. Mean-variance plot HUAWEI P9 Mean-variance plot generated using a series (ISO=3200) of unprocessed raw images ("snap-mode") acquired by a Huawei® P9 camera (blue points). The camera gain is constant up to a critical intensity of 220 ADU, which should not be exceeded in the experiment.

A series of ≈ 8000 images of dark background acquired in the video-mode with the Huawei® P9, automatically compressed with a H264 encoder, shows a problematic property. The mean of each dark frame over time (subset of 60 s) is shown in Fig. 7. It can be seen that the overall background drifts over time. This might be a thermal problem, although the signal is expected to rise rather than drop. This effect, however, might also be caused by the compression of the incoming signal. Unfortunately the Huawei® P9 has neither a temperature sensor on the chip nor a reproducible data compression, so the cause remains unclear. In addition, the signal drops periodically (every 1.07 s at 20 fps) which seems to be a compression artifact. A homogeneous although slightly noisy line would have been expected. The video acquisition exposes the drawback and limitations of the compression.

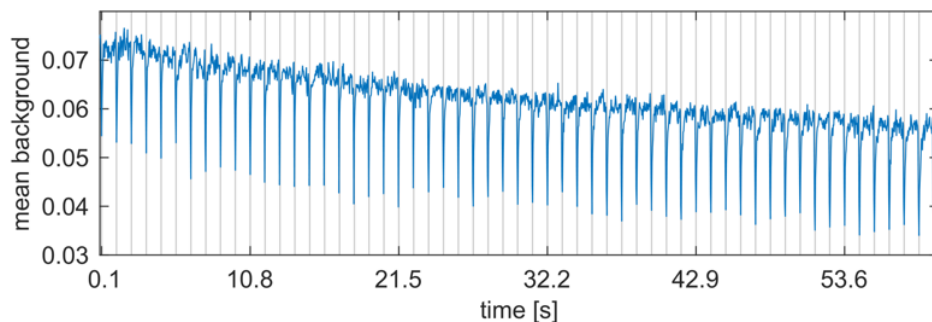


Figure 7. Mean of a dark image over time Mean of a dark image acquired with a Huawei® P9 camera and compressed with a H.264 encoder as a function over time. The overall decay of the signal and the periodic drop of the signal demonstrates the disadvantages of a compressed video signal. Equidistant gray lines (vertical) with 1.07 s (i.e. each 31st frame) at 29 *fps* spacing show the periodicity of the drop in the intensity signal. Certain pixel values less than a threshold are clipped to zero.

Looking at Fig 7 it can be seen that both the P9’s sensor and the video codec influence the saved image in a periodical but unpredictable manner. Settings like framerate and bitrate of the video-codec alter this effect. In addition, we observed that the dips depend on the number of photons. Thus, it is difficult to correct the compression artifacts of an unknown image.

Imaging techniques that require extensive image processing will have problems using such data. However, wide-field microscopy of bright specimens will be less affected. The localization accuracy of SMLM will be impaired the more noise each raw image contains.

However noise alone will not create artifacts. The occurring drop of the overall intensity is no problem either, because each image is processed individually and offset variations are automatically accounted for by rapidSTORM and ThunderSTORM.

D Neuronal Network Architecture and Training

In the beginning we used NNs to enhance the recorded image sequences which were then fed into common localization software like rapidSTORM [Wolter2012] and ThunderSTORM [Ovesny2014]. This has the advantage to benefit from the already existing and robust localization algorithms. Unfortunately this led to only minor improvements and in many cases actually to a deterioration of the reconstructed results, therefore we followed the approach from Nehme et al. [Nehme2018] to directly generate localization maps from the blinking fluorophores.

A Architecture

The network receives decoded and upsampled (e.g. $5\times$) video-frames x and their corresponding ground truth localization maps y .

The data-pairs (see Section D) were fed into our modified version of the image-to-image GAN network [Isola2016b], implemented in the open-source ML library Tensorflow [Abadi]. The code is based on the open-sourced version described in [Affinelay2018] and is publicly available [Diederich2018a]. To circumvent a checkerboard-like artifact resulting from the generator in the reconstruction process, we replaced the transposed-convolution operation in the decoding step of the U-NET [Ronneberger2015] by a resize-convolution layer as suggested in [Odena2016]. This in combination with longer training procedure eliminates high-frequency patterns due to the low coverage of the convolutions in the deconvolution process of the U-NET.

The floating-point localization table is generated by converting pixel-values greater than $0.3 \cdot \max(I_{frame})$ into effective pixel-dimensions.

B Training

The neural network (NN) was trained on a Nvidia Titan X GPU over fifteen thousand samples (input-size 256×256) with equal acquisition parameters corresponding to the d STORM experiment based on methods presented in Methods D.1 and D.2. Data was mixed in equal parts (i.e. 50%/50%) to not only learn the model of ThunderSTORM. We use minibatch stochastic gradient descent (SGD) and relied on the ADAM optimization scheme [Kingma2015] with learning rate of $1 \cdot 10^{-4}$ and momentum of $\beta = 0.25$. Our experiment showed, that the training converged to equilibrium after 10 epochs at a batch-size of 4 frames, which took about 3h time-effort on an ordinary desktop machine with 64Gb RAM, Intel Xeon

octacore and a Nvidia TitanX graphics card with 12GB memory. It is worth noting, that a precise alignment of the data is crucial, otherwise the recovered events will be shifted by an unknown amount and the localization fails due to smeared-out blinking events.

C Cost-Function

Following the original Pix2Pix-approach in [Isola2016b], the conditional GAN-loss can be expressed as

$$\mathfrak{L}_{cGAN}(G, D) = \mathbb{E}_{x,y} [\log(D(x, y))] + \mathbb{E}_x [1 - \log(1 - D(x, G(x)))] \quad (1)$$

where x gives the degraded video-frame and y the input ground truth images. G corresponds to the U-NET generator which tries to map the input image x together with random noise z to the recovered output-frame x ; $G : \{x\} \rightarrow y$. The discriminator D has to distinguish between real or fake (e.g. produced by the generator) samples. Additionally the \mathbb{L}_1 -norm is given as

$$\mathbb{L}_1(G) = \mathbb{E}_{x,y} [\|y - G(x)\|_1]. \quad (2)$$

For stable training with faster convergence, we convolved the fluorophore location maps (indicated as intensity peaks) in input y , as well as the generated predictions y' with a Gaussian PSF of experimentally individually determined radius and intensity. Thus

$$\mathbb{L}_1(G) = \lambda_{L1} \mathbb{E}_{x,y} [\|y \otimes PSF - G(x) \otimes PSF\|_1]. \quad (3)$$

To promote the sparsity in each frame produced by the generator, we add an additional \mathbb{L}_1 loss

$$\mathbb{L}_{1s}(x) = \lambda_{L1s} \|G(x)\|_{L1}. \quad (4)$$

Thus the final loss-function is given by

$$\mathbb{G} = \arg \min_G \max_D \lambda_{cGAN} \cdot \mathfrak{L}_{cGAN}(G, D) + \lambda_{L1} \cdot \mathbb{L}_1(G) + \lambda_{L1s} \cdot \mathbb{L}_{1s}(x). \quad (5)$$

Additional hyper-parameters λ_{cGAN} , λ_{L1} and λ_{L1s} are controlling the influence for each error term. The values for $\lambda_{cGAN} = 3$, $\lambda_{L1} = 100$, $\lambda_{L1s} = 100$ were chosen empirically, where we kept $\lambda_{cGAN} = 0$ for the first 1000 and then every third iterations to reduce any exploding gradients while training.

Compared to the Deep-STORM by Nehme et al. [Nehme2018], the here presented GAN architecture is more flexible in terms of the cost-function. This is because it holds a data-specific regularizer which learns the properties of the unpredictable camera compression while training the generator.

Instead the discriminator tries to distinguish whether the results are coming from the generator or from the GT dataset. Hence the GAN should come up with a learned forward model which successfully includes all unknown effects, especially the compression artifact, to find the center of each fluorophore. This facilitates a parameter free optimization technique, well suited for the unknown black-box by the cellphone camera.

D Generation of the training dataset

We used two different methods for a 50:50 mix of which generated the training dataset x to y to feed the modified version of the Pix2Pix GAN available at [Diederich2018a].

D.1 Dataset from camera’s model simulation

We first created a data-stack of simulated STORM frames using the software ThunderSTORM. Parameters for data-generation were selected in accordance to experimental conditions. In a later step we estimated a camera model, based on the properties determined in Methods C, to introduce noise into the data, before they were compressed by the H.264 video-codec in MATLAB [TheMathWorksInc.]. The compression ratio was tuned, so that the compression artifacts looked similar to the one from the original acquisition (“Video-Quality”: 80 – 90 %). The location of the H.264 integer blocks was not preserved when generating the dataset to avoid overfitting of the data due to the same grid-structure in each frame.

The compressed frames were decompressed and upsampled (e.g. $5\times$). The ThunderSTORM location positions were converted to the upsampled grid, rounded and a single pixel was set to the predicted brightness. This constituted the location maps.

Following this procedure gives only an estimated forward model of the unknown camera “black-box” and therefore cannot be expected to account for all properties of the data acquired by the cell-phone camera.

D.2 Dataset from localized dSTORM data

Our second way to generate a dataset was by taking captured *cell*STORM time-series using the video-mode from real biological cells (labeled microtubules) under optimal conditions. After localizing the blinking events using ThunderSTORM in each decoded frame, we extract the detected emitters and

generate a location map from this data.

To not only learn the forward model from the ThunderSTORM PSF-fitting algorithm, we also incorporated 50% data from the method described above. This makes the proposed methods more robust to variations in the data. It also successfully accounted for variations in sample's background as well as in the camera parameters.

E Testing

The GPU-based implementation of the localization image-generation algorithm allows fast multi-emitter processing and processes a video (e.g. 15 k frames, 128×128 pixels) at an upscaling-factor of 5 (to ensure sub-pixel super resolution) in about 5 Minutes (≈ 50 *fps*). On the other side the cellphone-based implementation can do 2-3 fps at 64×64 pixels input-frames, which can dramatically be increased by optimizing the code. Due to the convolutional-architecture of the PatchGAN-discriminator [Hou2015] it is possible to process data with frame-sizes different than the training dataset.

Our approach does not rely on any specific class of imaged objects, nor does it need any parameters other than a dataset which mimics the experimental data in the sense of acquisition parameters.